Available online at www.sciencedirect.com
SCIENCE DIRECT®
Remote Sensing of Environment 103 (2006) 338–350
Remote Sensing of Environment
www.elsevier.com/locate/rse

Spectral mixture analyses of hyperspectral data acquired using a tethered balloon

Xuexia Chen *, Lee Vierling [1]

Institute of Atmospheric Sciences, South Dakota School of Mines and Technology, Rapid City, SD 57701, USA

Received 23 April 2004; received in revised form 20 May 2005; accepted 21 May 2005

Abstract

Tethered balloon remote sensing platforms can be used to study radiometric issues in terrestrial ecosystems by effectively bridging the spatial gap between measurements made on the ground and those acquired via airplane or satellite. In this study, the Short Wave Aerostat-Mounted Imager (SWAMI) tethered balloon-mounted platform was utilized to evaluate linear and nonlinear spectral mixture analysis (SMA) for a grassland-conifer forest ecotone during the summer of 2003. Hyperspectral measurement of a 74-m diameter ground instantaneous field of view (GIFOV) attained by the SWAMI was studied. Hyperspectral spectra of four common endmembers, bare soil, grass, tree, and shadow, were collected in situ, and images captured via video camera were interpreted into accurate areal ground cover fractions for evaluating the mixture models. The comparison between the SWAMI spectrum and the spectrum derived by combining in situ spectral data with video-derived areal fractions indicated that nonlinear effects occurred in the near infrared (NIR) region, while nonlinear influences were minimal in the visible region. The evaluation of hyperspectral and multispectral mixture models indicated that nonlinear mixture model-derived areal fractions were sensitive to the model input data, while the linear mixture model performed more stably. Areal fractions of bare soil were overestimated in all models due to the increased radiance of bare soil resulting from side scattering of NIR radiation by adjacent grass and trees. Unmixing errors occurred mainly due to multiple scattering as well as close endmember spectral correlation. In addition, though an apparent endmember assemblage could be derived using linear approaches to yield low residual error, the tree and shade endmember fractions calculated using this technique were erroneous and therefore separate treatment of endmembers subject to high amounts of multiple scattering (i.e. shadows and trees) must be done with caution. Including the short wave infrared (SWIR) region in the hyperspectral and multispectral endmember data significantly reduced the Pearson correlation coefficient values among endmember spectra. Therefore, combination of visible, NIR, and SWIR information is likely to further improve the utility of SMA in understanding ecosystem structure and function and may help narrow uncertainties when utilizing remotely sensed data to extrapolate trace glas flux measurements from the canopy scale to the landscape scale.

Keywords: Spectral mixture analysis (SMA); Linear mixture model; Nonlinear mixture model; Endmembers; Short Wave Aerostat-Mounted Imager (SWAMI); Hyperspectral; Multispectral; Ponderosa pine; Tethered balloon

1. Introduction

1.1. Spectral mixture analysis

All land surfaces are spatially heterogeneous at some scale. As a result, most detected surfaces within the IFOV of the remote sensing instrument (herein referred to as a pixel), especially those detected by coarse spatial resolution instruments, are spectrally complex and therefore create a heterogeneous spectral mixture rather than one spectrally "pure" signal within the pixel. However, traditional classification methods often classify the whole pixel as a specific cover type assumed to represent the dominant component within

* Corresponding author. Current address: Science Applications International Corporation (SAIC), USGS National Center for Earth Resources Observation and Science (EROS), 47914 252nd Street, Sioux Falls, SD 57198, USA. Tel.: +1 605 594 2741.
E-mail addresses: xuchen@usgs.gov (X. Chen), leev@uidaho.edu (L. Vierling).
[1] Current address: College of Natural Resources, University of Idaho, Moscow, ID 83844, USA.

0034-4257/$ - see front matter © 2006 Elsevier Inc. All rights reserved.
doi:10.1016/j.rse.2005.05.023

the pixel, and stop short of providing additional information about the existence and relative fraction of additional cover types within the pixel. Thus, improving spectral unmixing techniques to quantify land cover types within pixels can greatly benefit surface land cover interpretation and generation of derivative land cover products. Due to the inherent heterogeneity of land surfaces, developing and validating spectral mixture analysis (SMA) techniques to study cover types at the subpixel scale is highly desirable for many applications regardless of the original pixel size. Benefits of sub-pixel land cover quantification range from improved ecosystem change detection (e.g. Monteiro et al., 2003) to potentially increasing our ability to correlate remote sensing data with exchanges of mass and energy between the biosphere and the atmosphere (see Chen et al., 1999; Ogunjemiyo et al., 2003). It may also improve our understanding of the biotic controls on these mass and energy exchanges and may allow us to partition the control of whole systems fluxes among cover types having different phenology.

SMA is an inverse method for deriving fractional coverage of spectrally distinct features within a pixel (Adams & Smith, 1986). In spectral mixture theory, the spectral signal of a pixel can be represented as a mixture of signals contributed by all spectrally "pure" features, or endmembers, within the instantaneous field of view (IFOV) of the sensor at a given time (Peddle et al., 1999; Sabol et al., 2002; Woodcock & Strahler, 1987). Theoretically, if all endmembers within an image can be identified and spectrally characterized, then the pixels may be characterized by how much of each endmember is contained within it. Practical applications of the spectral mixture models, however, are limited by the number of available spectral bands and the diversity among endmembers. High contrast endmembers (i.e. endmembers containing poor spectral correlation) are recommended to obtain spectral mixture models, and highly correlated endmembers should be avoided (Meer & Jong, 2000; Woodcock & Strahler, 1987) because they can exacerbate nonlinearities in spectral mixing and therefore cause uncertainty and error in SMA.

Much progress in spectral mixture techniques using remote sensing data has been made in recent years. Ground feature areal fraction information has been successfully provided by spectral mixture interpretation in many studies (e.g. Garcia-Haro et al., 1996; Jasinski & Eagleson, 1990; Kootwijk et al., 1995; Meer, 1995; Wessman et al., 1997). In addition, SMA theory has been used to quantify vegetation biomass, fraction of absorbed photosynthetically active radiation (FAPAR), leaf area index (LAI), and net primary productivity (NPP) (e.g. North, 2002; Peddle et al., 1999), and to map logging effects (e.g. Monteiro et al., 2003), snow cover (e.g. Painter et al., 1998; Vikhamar & Solberg, 2003), tree cover (e.g. Hansen et al., 2002), and impervious surfaces (e.g. Phinn et al., 2002; Ridd, 1995; Wu & Murray, 2003) in various applications. Clearly, further developments in SMA theory, including advances in error analyses, have the potential to affect studies across a wide range of environmental monitoring applications.

SMA techniques include both linear (e.g. Adams et al., 1995; Bastin, 1997; Foody & Cox, 1994; Meer, 1995; Peddle et al., 1999; Roberts et al., 1998; Rosin, 2001) and nonlinear (e.g. Borel & Gerstl, 1994; Huang & Townshend, 2003; Huete, 1986; Kootwijk et al., 1995; Ray & Murray, 1996; Roberts et al., 1993; Zhang et al., 1998) mixture approaches, each of which contains different levels of computational and conceptual complexity. If multiple scattering can be ignored, the mixed spectrum can be expressed by a linear combination of the endmember spectra based on their areal fractions. In nonlinear spectral mixture models, multiple scattering among components within the pixel is considered and mixed spectra are expressed using nonlinear contributions of multiple endmembers within the pixel. A nonlinear mixture model can better reduce residuals and improve unmixing accuracy, but its multiple scattering effects are not linearly correlated with the endmember areal fractions within the pixel. The greater complexity of nonlinear SMA methods, coupled with the non-intuitive interpretation of nonlinear SMA results (Kootwijk et al., 1995; Ray & Murray, 1996) underscores the need to evaluate both linear and nonlinear SMA approaches in a variety of vegetation structural types to determine their relative and absolute sources of error and uncertainty wherever possible.

Endmember collection and calibration are important in the application of SMA. In some laboratory and field spectral mixture experiments, the endmembers and the mixed signal had been acquired under common illumination and atmospheric conditions, and the calibration between them was not necessary (e.g. Borel & Gerstl, 1994; Ray & Murray, 1996; Zhang et al., 1998). In other applications on satellite or photographic images, image endmembers were selected from the image pixels directly, and again calibration was not necessary because the endmembers were in the same radiometric scale as the other pixels in the imagery. A third class of SMA applications have utilized laboratory collected or field collected reference endmembers to interpret the satellite imagery, with endmembers calibrated to the imagery so that the models could run correctly irrespective of differences in image/endmember acquisition radiometry (e.g. Adams & Smith, 1986; Adams et al., 1995; Sabol et al., 2002). Generally, reference endmembers contain higher purity than image endmembers, and they may produce higher accuracy or better understanding of the SMA. However, because of the uncertainty in pixel geolocation arising from radiometric and georegistration constraints of satellite data, it is difficult to quantify the performance of spectral unmixing techniques between image pixels and actual ground endmember fractional coverage in the field. Here, we introduce a field spectral sampling technique using a tethered balloon-mounted remote sensing system to evaluate linear and nonlinear SMA performance under a condition of high geometric precision over a forested ecosystem.

1.2. SWAMI platform

The orbital altitudes of IKONOS, Landsat ETM+, and MODIS satellite sensors are about 700 km, while the altitude of remote sensing-equipped aircraft is usually higher than 2 km due to safety considerations. To bridge the spatial gap between ground measures and satellite or aircraft measures, a hyperspectral remote sensing instrument platform called the Short Wave Aerostat-Mounted Imager (SWAMI) has been developed (Vierling et al., 2006-this issue). This platform can be attached to the tether line of a research balloon and used to measure the

hyperspectral reflectance of surface features using nested GIFOV sampling approaches from the ground up to approximately 2 km altitude above ground level. In addition, because tethered balloons have been used to quantify a variety of trace gas fluxes at the landscape scale [i.e. methane (Beswick et al., 1998; Choularton et al., 1995), non-methane hydrocarbons (Davis et al., 1994; Guenther et al., 1996; Greenberg et al., 1999; Spirig et al., 2004; Zimmerman et al., 1988), and carbon dioxide (Kuck et al., 2000)], employing quantitative radiometric instrumentation on such a platform opens new opportunities for comparing trace gas flux and spectral properties of vegetation at scales comparable to and larger than those measured by standard flux towers. Therefore, data acquired through platforms such as the SWAMI may be used to complement those data acquired through the tower-based Spectral Network (SpecNet) Working Group. Vierling et al. (2006-this issue) provide a detailed description of the SWAMI design, function, instrumentation, and potential applications.

Tethered balloons have been widely used for remote sensing purposes for over a century. Recently, true color and infrared aerial photographs taken from balloons or kites have been used in photography-based studies of periglacial features, vegetation growth, and soil properties (e.g. Boike & Yoshikawa, 2003; Buerkert et al., 1996; Friedli et al., 1998; Gerard et al., 1997). The study described in this paper, however, is the first time to our knowledge that a hyperspectral system has been flown from a tethered balloon in order to perform SMA. We attain a GIFOV comparable in area to four optical Landsat TM or ETM + pixels in order to study a conifer forest-grassland boundary where four endmembers (tree, grass, bare soil, and shadow) predominate.

In previous research, there has been little emphasis on evaluating linear and nonlinear models using data concurrently measured on the ground and from the air. High-resolution aerial photography (e.g. Elmore et al., 2000; Lobell et al., 2002; Small, 2001), Landsat data (e.g. Bastin, 1997; Foody & Cox, 1994), and lidar data (Chen et al., 2004) have been used to evaluate unmixing results in previous studies. In these methods, the atmospheric influences, geo-registration, and spatial resolution of imagery caused uncertainties in deriving the actual ground cover area fractions for evaluation. To reduce the uncertainties, we used the SWAMI platform to collect both spectral signals and ground video at a low altitude so that the effects of atmosphere, geo-registration, and spatial resolution were minimized. Thus, this study can provide higher accuracy and new understanding of different mixture models.

Additionally, the use of hyperspectral data in such a sampling scheme provides other potential benefits for SMA. The benefits of using hyperspectral data compared with multispectral satellite data are pronounced: (1) the endmembers can be characterized by their continuous spectra with high accuracy; (2) the performance of different models can be better understood when using continuous spectra as inputs; and (3) hyperspectral data may provide a higher degree of spectral separation among endmembers, therefore possibly reducing complications arising from unmixing ground components with similar spectral characteristics. Hyperspectral data can also be convolved to multispectral data to simulate satellite data performance, providing a more thorough understanding of how SMA models may perform using various orbiting sensors.

1.3. Objectives

The main goal of this study is to evaluate the performance of linear and nonlinear SMA over a conifer forest-grassland ecotone using unique spectral data and validation data collected both by the SWAMI platform and via ground-based measurement. Four key questions are addressed in this paper: (1) does spectral mixture occur linearly and/or nonlinearly at the subpixel scale of an open forest/grassland ecotone?; (2) at what accuracy can the linear and nonlinear models predict the ground component fractions with a given mixture signal?; (3) how much residual error occurs when linear and nonlinear models are used to interpret the areal fractions of different surface features?; and (4) can the reduced dimensionality of multispectral data be used to correctly interpret sub-pixel information in this ecosystem?

These specific study objectives complement our larger objective to develop tethered balloons into viable tools that can be used to establish and scale relationships between trace gas fluxes and surface radiometry (see Vierling et al., 2006-this issue). This goal is consistent with recent calls for the development of novel yet inexpensive sampling capabilities at intermediate scales (e.g. Gamon et al., 2004) and supports the scientific goals of the SpecNet community and related efforts. Aside from the fact that tethered balloons can carry instrumentation to quantify both fluxes (e.g. Greenberg et al., 1999) and surface reflectance (Vierling et al., 2006-this issue) across scales larger than those measured at flux towers, the spectral unmixing analyses presented here may help to extend recent methods of

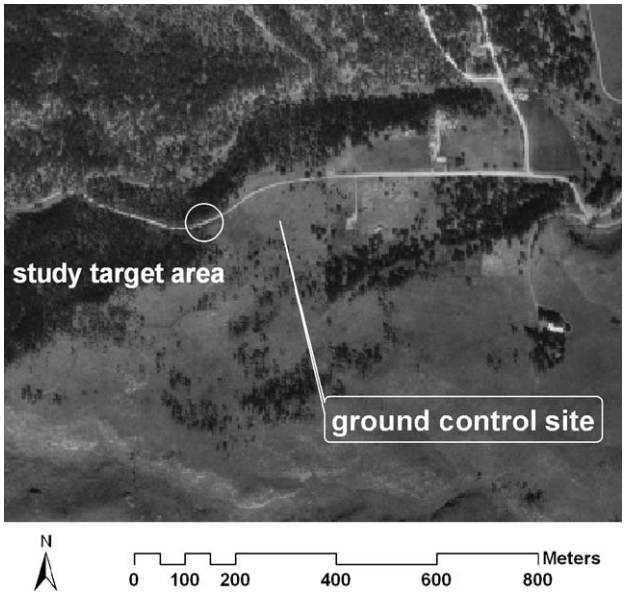

Fig. 1. Digital Orthophoto Quadrangle (DOQ) of study site. The GIFOV of SWAMI detected area in this study case is noted by white circle. Ground control center is located at 103.37°W, 44.08°N. The image was acquired from South Dakota Department of Environment and Natural Resources, Geological Survey.

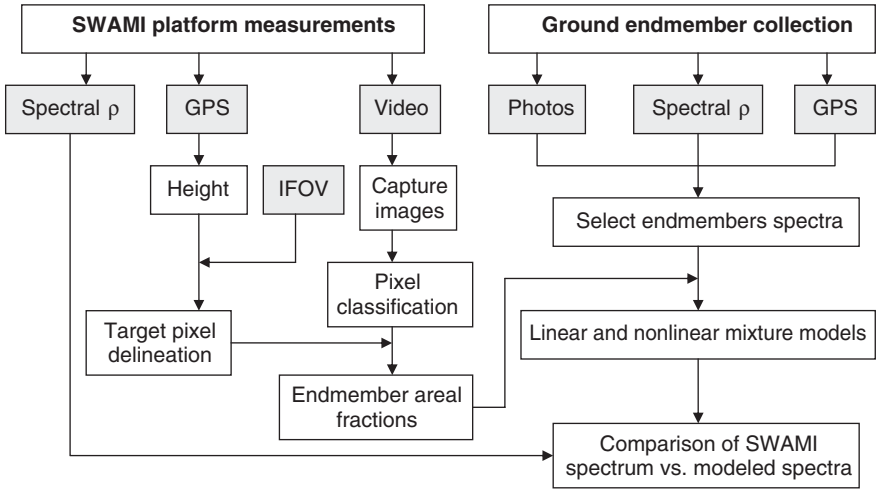

Fig. 2. The flow chart of data collection (noted by grey boxes) and data processing for SMA.

using whole-pixel vegetation classifications to better calibrate and predict trace gas fluxes (Chen et al., 1999; Ogunjemiyo et al., 2003) to the sub-pixel level.

2. Methods

2.1. Study area

Field experiments using the SWAMI platform were conducted in July 2003 in a forest/grassland ecotone west of Rapid City, South Dakota (Fig. 1). The study site is located in a topographically flat area (103.37°W, 44.08°N, elevation: 1287 m). The site is dominated by ponderosa pine (*Pinus ponderosa*) in the overstory, with the understory populated by various graminoids and short forbs.

2.2. Data acquisition

The Short Wave Aerostat-Mounted Imager (SWAMI) was used to collect surface spectral data in this study. The platform, mounted on a tethered balloon, contained a hyperspectral spectroradiometer (Fieldspec Dual UV/VNIR, Analytical Spectral Devices, Boulder, CO) with the 350 nm to 1050 nm detection region, a miniature color video camera (Supercircuits, Inc., Model PC169XS, Leander, TX) with 460 lines resolution, an OEM-grade global positioning system receiver (Model Svee Eight Plus, Trimble Navigation Ltd., Sunnyvale, CA), and other meteorological instrumentation (see Vierling et al., 2006-this issue). The GPS data and video signal were transferred to the ground via wireless modem for ground control adjustment. The flow chart of data collection and data processing is indicated in Fig. 2.

The altitude of the SWAMI platform was quantified using the GPS receiver. The color video was transferred to the ground and recorded on analog videotapes to identify the detected surface in the data processing; these images were later transferred to digital format for analysis. The dual UV/VNIR field spectroradiometer contained two fiberoptic cables; each leading to a different but commonly housed spectrometer. In this study, the downward pointing cable was fitted with an 18° foreoptic to record spectral surface radiance, while the upward pointing cable was fitted with a "remote cosine receptor" diffusing cap to measure solar irradiance. Real-time conversion of raw digital number to radiance or irradiance was accomplished using calibration coefficients provided by the manufacturer.

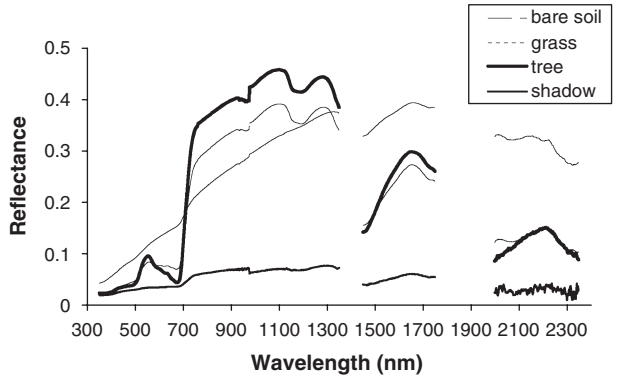

Fig. 3. Ground endmembers collected by FR field spectroradiometer. Regions seriously influenced by atmosphere were removed.

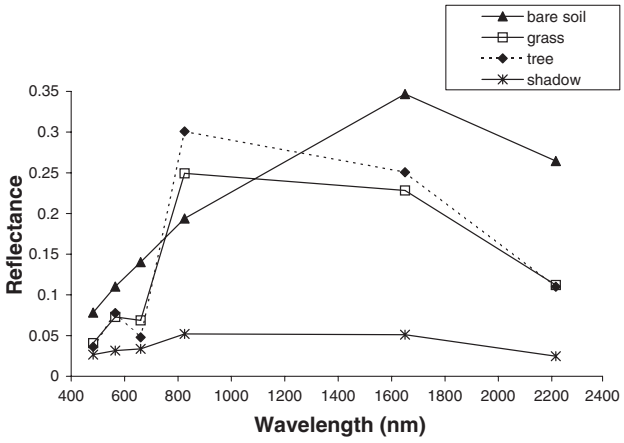

Fig. 4. Simulated Landsat 7 multispectral endmembers.

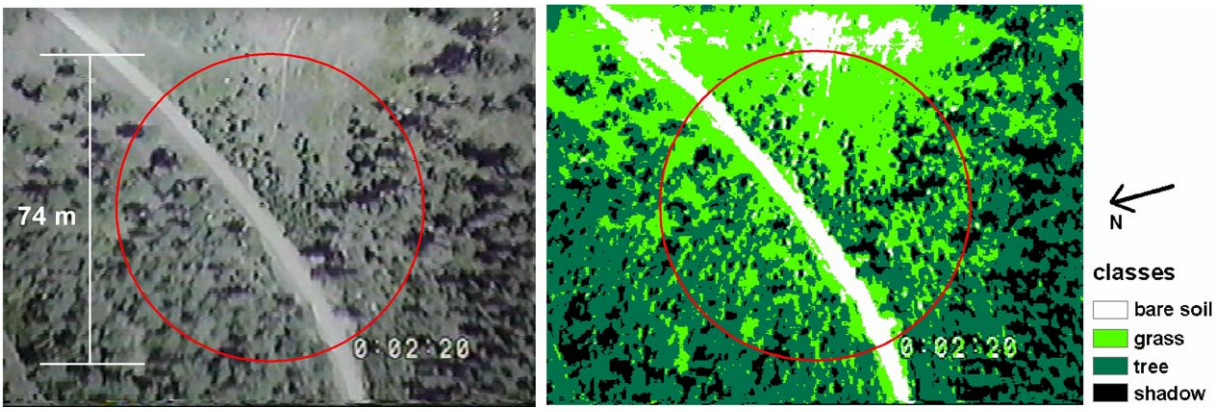

Fig. 5. Captured base image and classified image denoting spectroradiometer GIFOVs with circles.

The spectroradiometer used two different fixed concave holographic reflective gratings that disperse the collected radiance and irradiance onto two fixed photodiode arrays. Each array had 512 individual detection elements so that all wavelengths were collected at the same time. The optical heads of the video camera and the downward pointing cable were carefully mounted to the platform in the same plane to ensure target co-location. In this study, the dual UV/VNIR spectroradiometer and the video camera were pointed and stabilized at nadir.

In this study, both radiance and irradiance data were collected at the same time on the SWAMI platform and were transferred to the ground, thus the reflectance spectra could be calculated on the ground in real time. Classification results of video images captured in a SWAMI spectrum collection period (20 s) were averaged due to the movement of the platform in that period.

In situ ground feature spectra, including tree, grass, bare soil, and shadow, were collected in the field using an Analytical Spectral Devices (Boulder, CO) FieldSpec Pro FR (350 to 2500 nm) at the time of SWAMI data acquisition in the sky. A white reference panel (spectralon) was measured prior to every endmember measurement to calculate reflectance data. The data used in this study were collected at approximately 13:40 local daylight time (solar noon = 13:00 LDT) under near cloudless conditions. GPS location and digital photos of each ground measurement were acquired for endmember data processing. The common wavelengths of the two spectroradiometers were cross-calibrated in the lab and the reflectance measurements of both instruments matched well. The endmembers collected on the ground by the FR spectroradiometer and the mixed spectra collected on the SWAMI platform by the dual UV/VNIR spectroradiometer were acquired over a short time period with similar illumination and atmospheric conditions, and thus did not require further calibration.

2.3. Spectral data for mixture analysis

In this field experiment, the SWAMI platform was flown from 13:37 to 15:00, with the maximum platform height of 1030 m above ground level (AGL). After examining the video to assess target stability and heterogeneity, we selected one SWAMI spectrum collected at 233 m AGL for SMA. The collection time of this spectrum was at 13:43. The spectral region of 400–900 nm was used for SMA due to its higher quality and better stability than other regions. The diameter of ground instantaneous field of view (GIFOV) of the SWAMI spectrum was 74 m. Within the spectrometer GIFOV, four major surface features (i.e. endmembers) occurred: trees (ponderosa pine), grass/forbs, bare soil, and shadow (including self-shaded trees as well as shadows cast on understory vegetation and bare soil).

More than 10 spectra of each major ground feature (tree, grass, bare soil, and shadow) were collected using the FR spectrometer. These spectra were collected in various locations under the SWAMI detection area to capture the natural variation within the target. Tree spectra were collected on the top of several young trees (2–3 m high) on the sunlit side. Photos captured at the measurement points indicated that the tree spectra include reflectance from the sunlit branches, some self-shadowing caused by clumped needles, and natural gaps between branches. Bare soil endmembers were collected over both a bare soil road and the bare ground between vegetated areas (Fig. 5). Grass endmembers were acquired over various sunlit understory grasses/forbs. The measured shadow endmembers included

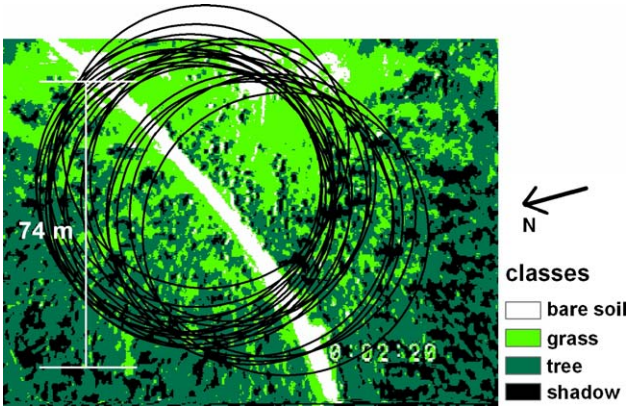

Fig. 6. Classified base image with GIFOVs denoted for each second during 20-s spectral collection period.

completely shaded tree, shaded understory grass/forbs, and shaded bare soil. At least four ground measurements of each endmember were selected from FR spectrometer measurements, and the averages of these spectra were taken to represent the endmember spectral signal. Each endmember spectrum therefore incorporated some of the variation inherent in each natural surface feature. The spectral ranges of these reference endmembers were 350–1350, 1450–1750, and 2000–2350 nm to exclude those regions seriously influenced by atmospheric absorption (Fig. 3). In this study, the tree endmember reflectance was slightly higher than the grass endmember reflectance in the green region because the understory grass had passed its period of maximum greenness and was much higher in the near infrared (NIR) region most likely caused by the difference in canopy structure between the trees and grass/forbs. However, because these two endmembers were highly correlated, additional SMA was conducted by combining the two green vegetation endmembers into one, along with retaining bare soil and shadow as additional endmembers. The endmember spectra from the 400 to 900 nm were used for the SMA in this study because those data coincided with the selected spectral range of the SWAMI instrument.

To better understand the potential unmixing performance of multispectral satellite data, the hyperspectral data of both endmembers and the SWAMI spectrum were converted into multispectral data using the spectral response functions of Landsat 7 ETM+ (Landsat 7 Science Data Users Handbook, http://ltpwww.gsfc.nasa.gov/IAS/handbook/handbook_toc.html) in six bands ranging from 450 to 515, 525 to 605, 630 to 690, 750 to 900, 1550 to 1750, and 2080 to 2350 nm, respectively. The endmembers of the six simulated Landsat bands centered at 482.5, 565, 660, 825, 1650, and 2215 nm are shown in Fig. 4. The first four bands were used for the SMA in this study due to the limited detection region of SWAMI spectra.

2.4. Spectral mixture models

A widely used simple linear spectral mixture model (e.g. Phinn et al., 2002; Schowengerdt, 1997; Theseira et al., 2002; Vikhamar and Solberg, 2003; Wu and Murray, 2003) was used in this study:

$$\rho_{mix} = \rho_t f_t + \rho_g f_g + \rho_b f_b + \rho_s f_s \quad (1)$$

where

$$f_t, f_g, f_b, f_s \geq 0, \text{ and } f_t + f_g + f_b + f_s = 1 \quad (2)$$

Here, ρ_{mix} is the calculated mixture spectrum using the linear mixture model; ρ_t, ρ_g, ρ_b, and ρ_s are the endmember spectra of tree, grass, bare soil, and shadow; and f_t, f_g, f_b, and f_s are the areal fractions of tree, grass, bare soil, and shadow endmembers within the detected surface. The sum of endmember areal fractions is equal to unity.

The difference ($\rho_{difference}$) between the mixture model (ρ_{mix}) and the real field measurement, SWAMI spectrum (ρ_{SWAMI}), is caused by the total residuals and unknown noise in the GIFOV as calculated using Eq. (3). The root-mean square error (RMSE, ρ_{RMSE}) is derived by Eq. (4) to evaluate the accuracy of the model, where S is the number of spectral bands.

$$\rho_{difference} = \rho_{mix} - \rho_{SWAMI} \quad (3)$$

$$\rho_{RMSE} = \sqrt{\frac{(\rho_{mix} - \rho_{SWAMI})^2}{S}} \quad (4)$$

Given endmember spectra and SWAMI spectrum, the endmember areal fractions f can be found by solving a constrained least squares problem (Eqs. (1) and (2)) with minimum error (Eq. (4)).

Though the linear mixture models may yield useful results, nonlinear models could better explain the effects of multiple scattering in complex vegetated surfaces (Borel & Gerstl, 1994; Theseira et al., 2002). Thus, a nonlinear spectral mixture model was used in this study to explore scattering influences. The nonlinear mixture model followed the format of previous nonlinear studies (e.g. Ray & Murray, 1996; Zhang et al., 1998). Considering the complexity of the four-endmember model, not all scattering effects were taken into account in this study. Due to the complexity of the tree canopies, the scattering relative to tree endmember, including the scattering between tree and tree ($\rho_t\rho_t$), grass and tree ($\rho_g\rho_t$), bare soil and tree ($\rho_b\rho_t$), and shadow and tree ($\rho_s\rho_t$), were assumed to be the most significant and were included in the nonlinear mixture model. We utilized the methodology described in Eqs. (5) (6) and (7) to calculate the nonlinear mixture within a pixel:

$$\rho_{mix} = \rho_t a_t + \rho_g a_g + \rho_b a_b + \rho_s a_s + \rho_t\rho_t b_{tt} + \rho_g\rho_t b_{gt} + \rho_b\rho_t b_{bt} + \rho_s\rho_t b_{st} \quad (5)$$

where

$$a_t,\ a_g,\ a_b,\ a_s,\ b_{tt},\ b_{gt},\ b_{bt},\ b_{st} \geq 0, \text{ and } a_t + a_g + a_b + a_s + b_{tt} + b_{gt} + b_{bt} + b_{st} = K \quad (6)$$

$$f_t = a_t/K,\ f_g = a_g/K,\ f_b = a_b/K,\ f_s = a_s/K,\ f_{tt} = b_{tt}/K,\ f_{gt} = b_{gt}/K,\ f_{bt} = b_{bt}/K,\ f_{st} = b_{st}/K \text{ and } f_t + f_g + f_b + f_s + f_{tt} + f_{gt} + f_{bt} + f_{st} = 1 \quad (7)$$

Here ρ_{mix} is the nonlinear model derived mixture spectrum; ρ_t, ρ_g, ρ_b, and ρ_s are the endmember spectra of tree, grass, bare soil,

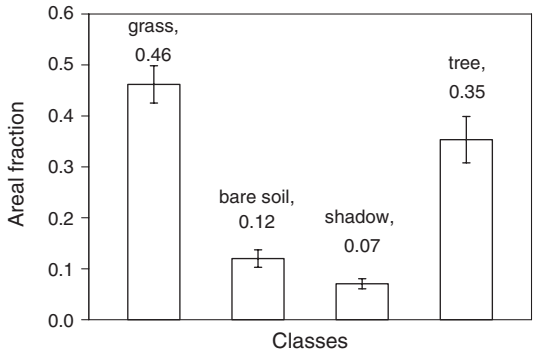

Fig. 7. Statistics of the classification results upon the base image in the 20-s collection period.

Table 1
Comparison of areal fractions (f) and error (ρ_{RMSE}) derived from all four-endmember spectral mixture models

Data	Models	Grass (f_g)	Bare soil (f_b)	Shade (f_s)	Tree (f_t)	Grass × tree (f_{gt})	Bare soil × tree (f_{bt})	Shadow × tree (f_{st})	Tree × tree (f_{tt})	Sum	Error (ρ_{RMSE})
Hyperspectral	(a) Validation data, linear mixture	0.46	0.12	0.07	0.35					1	0.054
	(b) Linear unmixing	0.46	0.16	0.35	0.03					1	0.003
	(c) Nonlinear unmixing	0.36	0.38	0	0.02	0	0	0	0.24	1	0.002
Multispectral	(d) Validation data, linear mixture	0.46	0.12	0.07	0.35					1	0.038
	(e) Linear unmixing	0.50	0.15	0.35	0					1	0.002
	(f) Nonlinear unmixing	0.24	0.30	0	0	0.14	0.12	0.08	0.12	1	0.000

and shadow. a_t, a_g, a_b, and a_s are the contribution factors of the first-order mixture (linear) effect of tree, grass, bare soil, and shadow endmembers while b_{tt}, b_{gt}, b_{bt}, and b_{st} are the contribution factors of the second-order mixture (multiple scattering influences) effect between tree and tree, grass and tree, bare soil and tree, and shadow and tree endmembers due to multiple scattering. K is the sum of all contribution factors. The areal fractions of different contribution items (f_t, f_g, f_b, f_s, f_{tt}, f_{gt}, f_{bt}, and f_{st}) are calculated using Eq. (7). The sum of areal fractions is equal to unity.

The difference ($\rho_{difference}$) and RMSE (ρ_{RMSE}) of the nonlinear model were also calculated using Eqs. (3) and (4). The solution of the endmember areal fractions was again derived by solving a constrained least squares problem (Eqs. (5) and (6)) at the point of minimum error (Eq. (4)).

A unique solution of endmember areal fractions can be interpreted by linear and nonlinear models as long as the number of spectral bands/channels plus one is equal to or larger than the number of endmembers. In this study, both field-collected hyperspectral data and simulated multispectral data were used to examine the linear and nonlinear models using spreadsheet software (Excel, Microsoft, Redmond WA).

2.5. Ground data used in model evaluation

The ground spectrum collected by the SWAMI platform occurred over a 20-s period, thus 20 surface images were captured from the video collected by the color camera in the frequency of one frame per second during the data collection period. The size of each captured image was 1024 × 768 pixels. Because it contained maximum overlap with all other images, the image captured at the 9th second was used as the base image. The base image was classified into four land cover types, including tree (sunlit tree), grass, bare soil, and shadow (including shadow on the ground and self-shaded trees) using a two-step process based on the blue, green, and red brightness. In the first image classification step, the maximum likelihood method was used to classify the image into three land cover classes: grass, bare soil, and tree/shade. Because the similar brightness values of tree and shadow precluded separating these two classes, a second step was then made in which classes originally designated as grass and bare soil were masked from the original image, and then a minimum distance method was used to separate the tree, shade, and grass which were previously misclassified as tree/shade. The final classification result was visually compared with the original image (Fig. 5) and was considered an accurate classification of the ground feature fractional coverages.

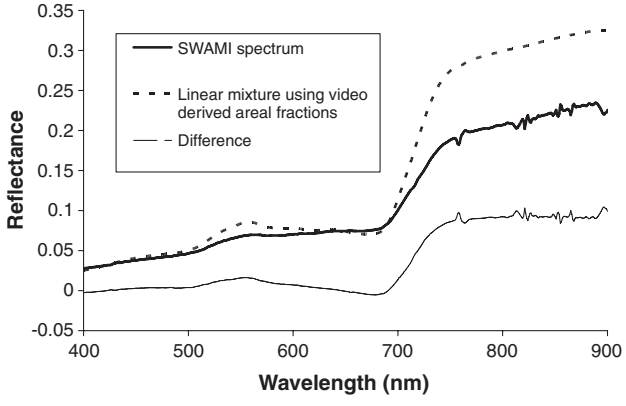

Fig. 8. Comparison of linear mixture using validation data vs. field-collected SWAMI spectrum.

The view centers of the other 19 images were registered with the base image, and their GIFOVs were denoted on the base image (Fig. 6). Statistical analyses of endmember areal fractions were performed for these 20 GIFOVs based on the classification result of the base image. Using the overlap of the 19 images with the base image, we were able to characterize the footprint with very good geometric control, with >99% of the classified ground area quantified by SWAMI hyperspectral measures (see GIFOV circle overlaps with base image in Fig. 6). The average endmember fractions of grass, bare soil, shadow, and tree in the collection period were 0.46, 0.12, 0.07, and 0.35, respectively (Fig. 7). These data were used as validation data of endmember areal fractions in order to evaluate the different spectral mixture models (Table 1).

3. Results

3.1. Spectral mixture analysis using hyperspectral data

Ground validation data of endmember areal fractions (Fig. 7) derived from the classification results of images captured by video were used as the inputs of endmember fractions in Eq. (1) to calculate linear mixture signals. The calculated mixture spectrum was compared with the SWAMI spectrum (Fig. 8). The difference between the linear mixture spectrum and the SWAMI spectrum indicated that the linear spectral mixture derived from validation data matched well in the visible region (400–700 nm) but

separated greatly in the NIR region (700–900 nm) where multiple scattering produced nonlinear effects. Other potential reasons for this discrepancy in the NIR region might be due to atmospheric effects (X. Chen and L. Vierling, unpublished results) and the selection of two vegetation endmembers. The RMSE of the linear mixture result was 0.054 [shown in Table 1, (a)] and represented the maximum amount of error when compared with other models.

By evaluating hyperspectral endmember spectra and the SWAMI-acquired spectrum using the linear mixture model, endmember areal fractions were interpreted. The difference and error between the model-derived spectrum and the measured SWAMI spectrum was significantly reduced relative to the first model run where the model used ground validation data as inputs [Table 1, (b), Fig. 9]. The nonlinear model derived mixture spectrum and the areal fractions using four endmembers and the SWAMI spectra are indicated in Fig. 10 and Table 1, (c). The nonlinear model contained less difference and error than the two application cases of linear model described above.

The endmember areal fractions of grass and bare soil derived from the linear model (0.46 and 0.16, respectively) were close to the validation data derived from the GIFOV image classification results (0.46 and 0.12, respectively). The linear model significantly overestimated the shadow fraction as 0.35 and underestimated the tree fraction as 0.03 [Table 1, (b)]. This is likely due to the high correlation of endmembers and the significant scattering that occurred within plant canopies in the NIR.

The areal fractions derived using the nonlinear model indicate that the areal fractions from grass and bare soil were similar (0.36 and 0.38, respectively), while the areal fractions of tree and shadow endmembers were low (0 and 0.02, respectively) [Table 1, (c)]. The multiple scattering between tree and tree endmembers was significant (f_{tt}=0.24), whereas the contributions of other scattering influences were zero. The bare soil areal fraction (0.38) was approximately a factor of 3 higher than the validation data (0.12), and the other endmembers varied from the validation data to different extents.

The above analyses indicate that, on one hand, both linear and nonlinear mixture models can be used to calculate spectral mixture performance with low errors in spectral differences between modeled and measured spectra. However, some model derived endmember areal fractions varied greatly from the validation data. Of particular note is that although endmember

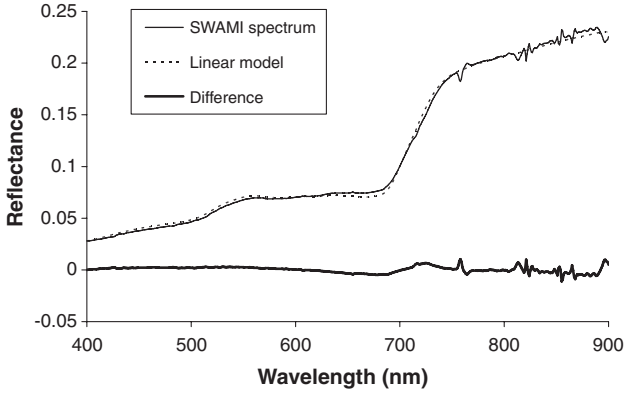

Fig. 9. Comparison of linear model vs. field-collected SWAMI spectrum.

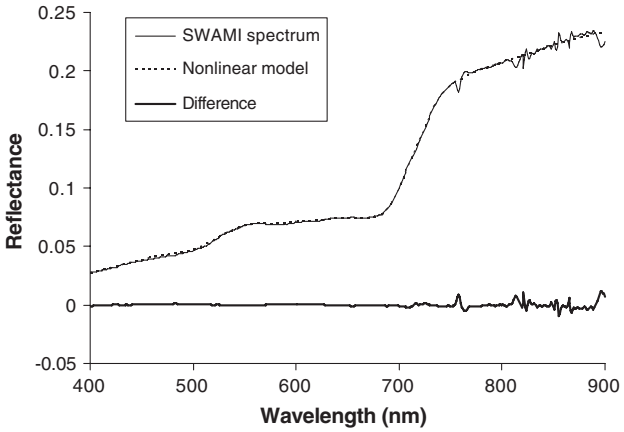

Fig. 10. Comparison of nonlinear model vs. field-collected SWAMI spectrum.

fractions could be calculated with a low error term using the linear approach [Table 1, (b)], the derived fractions of tree and shade differed substantially from the actual validation data. Thus, in using linear SMA in such a forested conifer ecosystem, much caution is in order if one tries to separate the shade and tree endmembers (see also Chen et al., 2004). Further studies are needed to improve the models and better interpret the results into the real ground endmember fractions, particularly where nonlinear scattering effects are prevalent.

3.2. SMA using simulated multispectral Landsat 7 data

In many studies, it may not be possible to acquire hyperspectral data collected via spaceborne (e.g. Hyperion), airborne (e.g. the Airborne Visible Infrared Imaging Spectrometer, AVIRIS) or field instruments. SMA has been widely applied to multispectral Landsat data (e.g. Adams et al., 1995; Casals-carrasco et al., 2000; Monteiro et al., 2003; Peterson & Stow, 2003; Sabol et al., 2002; Small, 2001; Wu & Murray, 2003); thus simulated multispectral Landsat 7 data were used for SMA in this study to examine the models with these data sets of lower spectral dimensionality. Both multispectral endmembers and SWAMI GIFOV data contained four bands, including blue, green, red, and NIR, centered at 482.5, 565, 660, and 825 nm, respectively. The mixture signal calculated using areal fractions of validation data was compared with the SWAMI spectrum in Fig. 11 and Table 1,

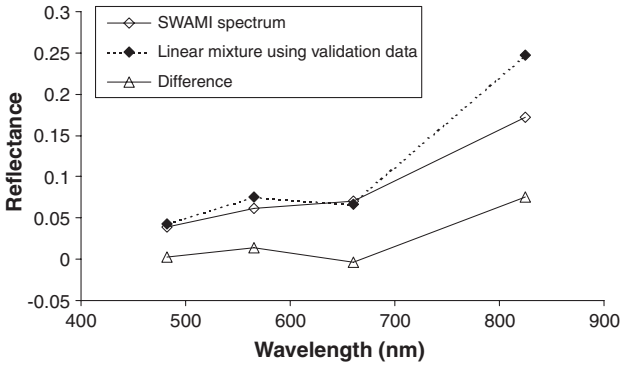

Fig. 11. Comparison of multispectral linear mixture using validation data vs. field-collected SWAMI spectrum.

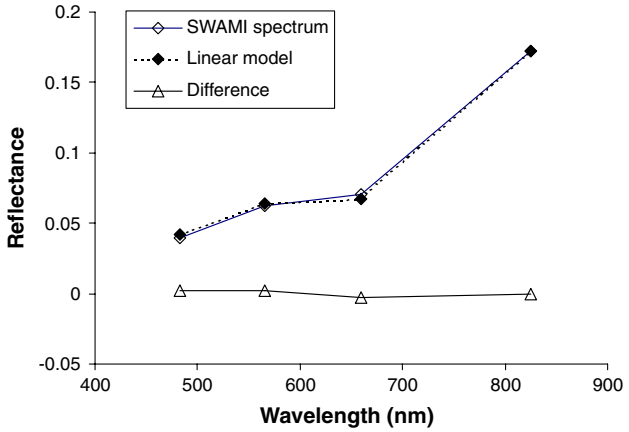

Fig. 12. Comparison of multispectral linear model vs. field-collected SWAMI spectrum.

(d). The mixture results matched well with SWAMI measurements in blue, green and red bands, yet varied greatly in the NIR band with a difference of about 0.08 (Fig. 11). The endmember areal fractions derived by the linear and nonlinear models are shown in Table 1, (e) and (f) and their spectra were compared with the SWAMI spectrum (Figs. 12 and 13, respectively). Both models contained much lower errors than the multispectral linear mixture using areal fractions of validation data [Table 1, (d)]. The linear model-derived grass and bare soil endmember fractions (0.50 and 0.15, respectively) were close to the validation data (0.46 and 0.12, respectively) while the estimation of shade and tree (0.35 and 0, respectively) varied greatly from the validation data (0.07 and 0.35, respectively). These results were similar to the hyperspectral analysis results.

The multispectral nonlinear model-derived results [Table 1, (f)] indicate that the contribution of the scattering between grass and tree was 0.14, which was slightly higher than the other three scattering influences between bare soil and tree (0.12), tree and tree (0.12), and shadow and tree (0.08). The multispectral nonlinear model derived areal fractions of grass, bare soil, shade and tree endmembers (0.24 and 0.30, 0, and 0, respectively) substantially varied from the validation data (0.46, 0.12, 0.07, and 0.35, respectively) [Table 1, (f) and (d)].

The above hyperspectral and multispectral mixture analyses indicate that the linear model is more stable than the nonlinear model in this system. The results of linear models were similar in both hyperspectral and multispectral data [Table 1, (b) and (e)]. In contrast, the nonlinear model considered not only the linear contribution of endmembers, but also the multiple scattering influences among endmembers, thus the nonlinear model was sensitive to different data sets and the SMA results of hyperspectral and multispectral data sets were greatly different [Table 1, (c) and (f)]. In addition, most linear/nonlinear model-derived endmember fractions varied from the validation data to some extent and these differences were sometimes substantial (Table 1).

3.3. Correlation of endmembers

Surface features exhibit distinct and characteristic variations in spectral radiance (e.g. Figs. 3 and 4). However, it is intuitive that the more spectral correlation that occurs among endmembers, the more difficult it will be to discriminate endmember fractions using SMA. The Pearson correlation coefficient and *P*-value statistics for hyperspectral and multispectral endmembers are shown in Table 2. The shade endmember had a high correlation with the other three endmembers. Grass and tree were both green vegetation, and they had very similar spectra (Fig. 3). Both of them had low reflectance in red and high reflectance in NIR, and their Pearson correlation parameters ($R=0.996$ and 0.994 for full range hyperspectral and multispectral data, respectively) were higher than other R values (Table 2). Bare soil contained lower correlations with grass, tree, and shadow endmembers compared with the correlations among those three endmembers. The high correlations of the four endmembers in the 400–900 nm region likely caused high errors in the above spectral mixture models.

Table 2 shows that the R value of shadow and bare soil decreased from 0.98 to 0.51 when the hyperspectral region extended from 400–900 nm to 350–2350 nm. Including short wave infrared (SWIR) in the endmembers can effectively reduce the R values among endmembers; thus, the SMA results could be improved by including full range endmembers that were less closely correlated with each other. Future unmixing efforts in such ecosystems will benefit from the incorporation of SWIR bands.

3.4. Re-selection of endmembers

Highly correlated endmembers can cause error in spectral mixture models (Theseira et al., 2002). Meer and Jong (2000) found that the use of poorly correlated endmembers improved SMA-derived cover estimates relative to when endmembers were highly correlated. For this reason, in some previous studies, shadow was not considered as an individual endmember (e.g. Chen et al., 2004; Lobell et al., 2002) and both grass and tree were included in a green vegetation endmember (e.g. Adams et al., 1995; Asner & Lobell, 2000). To examine the influence of endmember selection on SMA in this study, we re-selected endmembers for the analysis area. The grass and tree endmembers were linearly combined as one vegetation endmember

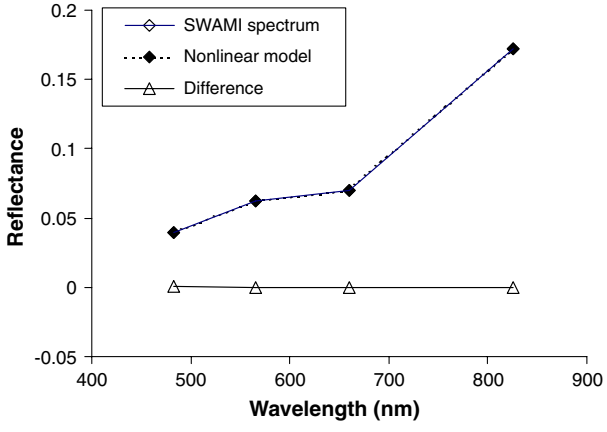

Fig. 13. Comparison of multispectral nonlinear model vs. field-collected SWAMI spectrum.

Table 2
Pearson correlation (R values) and P values of hyperspectral and multispectral endmembers

	Hyperspectral (400–900 nm)			Hyperspectral (350–2350 nm)			Multispectral (4 bands)			Multispectral (6 bands)		
	Bare soil	Grass	Tree	Bare soil	Grass	Tree	Bare soil	Grass	Tree	Bare soil	Grass	Tree
Grass	0.957			0.641			0.910			0.715		
	0.000			0.000			0.090			0.110		
Tree	0.935	0.997		0.580	0.996		0.870	0.996		0.652	0.994	
	0.000	0.000		0.000	0.000		0.130	0.004		0.160	0.000	
Shadow	0.980	0.994	0.984	0.510	0.955	0.958	0.961	0.989	0.972	0.512	0.909	0.905
	0.000	0.000	0.000	0.000	0.000	0.000	0.039	0.011	0.028	0.299	0.012	0.013

using their various fractions detected on the video images (Figs. 3 and 7, and Eq. (8)).

$$\rho_v = (0.35\rho_t + 0.46\rho_g)/(0.35 + 0.46) \quad (8)$$

Here ρ_v, ρ_t, and ρ_g are the endmember spectra of vegetation, tree, and grass, respectively.

The linear and nonlinear SMA models on three endmembers were similar to those on four endmembers described in Eqs. (1)–(7). In the three-endmember nonlinear model, all scattering influences among three endmembers were considered (Eq. (9)):

$$\rho_{mix} = \rho_v a_v + \rho_b a_b + \rho_s a_s + \rho_v \rho_s b_{vs} + \rho_v \rho_b b_{vb} + \rho_b \rho_s b_{bs} \quad (9)$$

Here ρ_{mix} is the nonlinear model-derived mixture spectrum; ρ_v, ρ_b, and ρ_s are the endmember spectra of vegetation, bare soil, and shadow. a_v, a_b, and a_s are the contribution factors of the first-order mixture (linear) effect of vegetation, bare soil, and shadow endmembers while b_{vs}, b_{vb}, and b_{bs} are the contribution factors of the second-order mixture (multiple scattering influences) effect of vegetation, bare soil, and shadow endmembers due to multiple scattering. The equations used to calculate the areal fractions of vegetation (f_v), bare soil (f_b), shadow (f_s), and the scattering items (f_{vb}, f_{vs}, and f_{bs}) were similar to Eqs. (6) and (7).

The linear and nonlinear analyses of both hyperspectral and multispectral data were performed using the vegetation, bare soil, and shade endmembers and the results are listed in Table 3. Most model-derived areal fractions still varied greatly from the validation data despite endmember reselection. The unmixing results of the linear model using hyperspectral and multispectral data were very stable [Table 3, (b) and (e)], while the results of the nonlinear model varied greatly [Table 3, (c) and (f)]. The nonlinear multispectral SMA model [Table 3, (f)] derived areal fractions of bare soil and shade endmembers (0.13 and 0.06, respectively) were very close to the validation data (0.12 and 0.07, respectively). Almost all multiple scattering influences (f_{vb}, f_{vs}, and f_{bs}) were relative to sunlit vegetation or shaded vegetation, thus these contributions were added to the vegetation fraction (f_v) item. The summed areal fraction (0.81) is equal to the validation data (0.81). This result indicated that with appropriate endmembers and the appropriate SMA model, surface areal fractions could be calculated correctly. In other words, the SMA method remains highly subject to user bias in endmember choice.

4. Discussion and conclusion

SMA interprets areal fractions of surface features within a pixel, unlike vegetation indices, which express the overall information without abundance information of surface features within that pixel. Successfully detecting the fractional abundances of surface features cannot only be useful for interpreting biophysical parameters for quantifying the land cover such as biomass and LAI estimation, vegetated area, snow-cover area, and impervious area (e.g. Hansen et al., 2002; North, 2002; Peddle et al., 1999; Phinn et al., 2002; Vikhamar & Solberg, 2003; Wu & Murray, 2003), but can also capture the human effects on land use that are difficult to interpret directly from vegetation indices. A comparison of vegetation indices and SMA by North (2002) indicated that SMA improved vegetation cover estimates made using vegetation indices. SMA techniques may prove useful when comparing remote sensing measurements to flux tower measurements in real time, due to the fact that fluxes of CO_2, water vapor, and other trace gases can relate strongly to plant functional groups due to differences in light availability, plant water status, and other

Table 3
Comparison of areal fractions (f) and error (ρ_{RMSE}) derived from all three-endmember spectral mixture models

Data	Models	Vegetation (f_v)	Bare soil (f_b)	Shade (f_s)	Vegetation × bare soil (f_{vb})	Vegetation × shade (f_{vs})	Bare soil × shadow (f_{bs})	Sum	Error (ρ_{RMSE})
Hyperspectral	(a) Validation data, linear mixture	0.81	0.12	0.07				1	0.054
	(b) Linear unmixing	0.42	0.21	0.37				1	0.003
	(c) Nonlinear unmixing	0.13	0.16	0	0.03	0.62	0.06	1	0.002
Multispectral	(d) Validation data, linear mixture	0.81	0.12	0.07				1	0.038
	(e) Linear unmixing	0.41	0.21	0.38				1	0.003
	(f) Nonlinear unmixing	0.06	0.13	0.06	0.39	0.11	0.25	1	0.000

ecophysiological considerations (e.g. Gamon et al., 2004; Guenther, 1997). This point underscores the need for improved SMA methodology when relating vegetation reflectance data with ecosystem trace gas flux over heterogeneous and discontinuous canopies where the understory receives a substantial fraction of available sunlight. Because trace gas fluxes are driven by processes occurring at the sub-pixel level in heterogeneous canopies, such multi-scale analyses are of importance to the goals of the SpecNet community which includes the use of remote sensing to understand the contributions of various functional types or cover classes to fluxes. Continued work to spatially differentiate endmembers that are highly *spectrally* correlated (e.g. grass and tree fractions in this study), yet poorly related in their *ecophysiological function* (particularly true, in this case, for grasses and conifer tree species), will help to narrow uncertainties in measuring trace gas fluxes using spectral information.

In some previous SMA research using field-based hyperspectral data, only two surface features were considered in the comparison of linear and nonlinear mixture models, due to the complexity of the nonlinear scattering and limitation of the data collection (e.g. Borel & Gerstl, 1994; Ray & Murray, 1996; Zhang et al., 1998). In the current study, a tethered balloon platform was used for the first time to evaluate SMA in a conifer forest using four common surface features: bare soil, grass, tree, and shadow. This SWAMI field experiment provided unique data that illustrate the significant challenges inherent in SMA analysis for achieving reliable, quantitatively defensible results. The linear mixture calculated by validation data (Figs. 8 and 11)) showed that nonlinear scattering influences were significant in the NIR and were less influential in the visible region, which agreed with previous results provided by Roberts et al. (1993), Gilabert et al. (2000), and Lobell et al. (2002). Lobell et al. (2002) found that weakly anisotropic reflectance occurred in the NIR, while strongly anisotropic reflectance occurred in the visible region due to the high transmittance and reflectance of NIR photons and high absorption of photons in visible region by most surface features. Though the simplified nonlinear models used in this study were not fully conclusive, they did represent new efforts towards understanding nonlinear effects in a heterogeneous canopy using co-located data attainable using the SWAMI platform and sampling design. This study suggested that using full range endmembers with less correlation with each other could improve the classification accuracy and address some of the limitation in SMA. We anticipate that further improvements in the SWAMI platform and sampling design, including continued field-based research on SMA in the context of biosphere–atmosphere fluxes, will benefit the research goals of the FLUXNET and SpecNet communities.

Though both the model-derived linear and nonlinear mixture spectra highly matched the SWAMI spectrum, most derived areal fractions of endmembers varied considerably from the validation data. The uncertainty of endmember fraction estimation from mixture models has been demonstrated in previous research when evaluated with reference data (e.g. Chen et al., 2004; Lobell et al., 2002; Rosin, 2001; Small, 2001). The results of the present study demonstrate that shadow and vegetation endmembers were difficult to successfully predict by linear model due to the high correlation and multiple scattering influences of endmembers. Both linear and nonlinear mixture models overestimated the areal fraction of bare soil (Tables 1 and 2), which also occurred in Rosin's (2001) spectral mixture model. According to Gilabert et al. (2000), bare soil reflectance can be influenced by adjacent cover types such as plants; overestimation of bare soil occurs due to the increased bare soil reflectance signal caused by significant side scattering influences in the NIR. The comparison of hyperspectral and multispectral SMA models indicated that the nonlinear model was sensitive to the hyperspectral and multispectral data, while the linear model was more stable when using these different sets.

In addition to the significant influence of multiple scattering, the spectral correlation of endmembers was presumably one of the sources of error in the SMA. In this study, the four endmembers (tree, grass, bare soil, and shadow) were highly correlated in the region of the 400–900 nm (Table 2) thus some model-derived areal fractions varied greatly from the validation data. The SMA of three endmembers (vegetation, bare soil, and shadow) was performed and the nonlinear multispectral model derived areal fractions matched well with the validation data in some cases [Table 3, (f)]. This significant improvement could be due to several reasons. First, the re-selection of endmembers had reduced the correlations significantly. Secondly, the SMA benefited from considering multiple scattering influences between endmembers. Finally, using the Landsat 7 multispectral response functions could capture the dominant spectral characteristics and exclude the spectral regions containing less information and higher error.

Research by Asner and Lobell (2000) and Lobell et al. (2002) demonstrated that SWIR reflectance could be used to successfully interpret the subpixel information of vegetation and soil due to their spectral dissimilarity in these wavelength regions. In this study, including SWIR significantly reduced the Pearson correlation values (Table 2) between endmembers. Combination of visible and SWIR information is likely to improve endmember estimation using spectral mixture models in future studies, particularly when using SMA to distinguish vegetation functional groups. Furthermore, because vegetation SWIR reflectance has been shown to be sensitive to vegetation water status (e.g. Carter, 1991), use of these wavebands may also further the goals of the SpecNet community in linking reflectance spectra with ecophysiological function related to biosphere–atmosphere trace gas exchange. Therefore, future studies to link structural characteristics (e.g. vegetation functional groups) and functional characteristics (e.g. biosphere–atmosphere mass and energy fluxes) of ecosystems using remote sensing data will benefit from the inclusion of these wave bands in the measurement design.

Acknowledgements

This research work was funded by National Science Foundation grant DBI-9985039, L. Vierling, PI. We thank M. Fersdahl for providing comments on the manuscript and for assisting with spectral endmember collection in the field; and P. Zimmerman for assistance with balloon logistics and flight. We

also thank E. Duke for the use of his ASD FieldSpec FR instrument and SWAMI group members for efforts on the design, construction, and flight of the SWAMI platform. John Gamon and two anonymous reviewers provided much appreciated comments on an earlier version of this manuscript.

References

Adams, J. B., Sabol, D. E., Kapos, V., Filho, R. A., Roberts, D. A., Smith, M. O., et al. (1995). Classification of multispectral images based on fractions of endmembers: Application to land-cover change in the Brazilian Amazon. *Remote Sensing of Environment*, *52*, 137−154.

Adams, J. B., & Smith, M. O. (1986). Spectral mixture modeling: A new analysis of rock and soil types at the Viking lander 1 Site. *Journal of Geophysical Research*, *91*, 8098−8112.

Asner, G. P., & Lobell, D. B. (2000). A biogeophysical approach for automated SWIR unmixing of soils and vegetation. *Remote Sensing of Environment*, *74*, 99−112.

Bastin, L. (1997). Comparison of fuzzy c-means classification, linear mixture modeling and MLC probabilities as tools for unmixing coarse pixels. *International Journal of Remote Sensing*, *18*, 3629−3648.

Beswick, K. M., Simpson, T. W., Fowler, D., Choularton, T. W., Gallagher, M. W., Hargreaves, K. J., et al. (1998). Methane emissions on large scales. *Atmospheric Environment*, *32*(19), 3283−3298.

Boike, J., & Yoshikawa, K. (2003). Mapping of periglacial geomorphology using kite/balloon aerial photography. *Permafrost and Periglacial Processes*, *14*, 81−85.

Borel, C. C., & Gerstl, S. A. W. (1994). Nonlinear spectral mixing models for vegetative and soil surfaces. *Remote Sensing of Environment*, *47*, 403−416.

Buerkert, A., Mahler, F., & Marschner, H. (1996). Soil productivity management and plant growth in the Sahel: Potential of an aerial monitoring technique. *Plant and Soil*, *180*, 29−38.

Carter, G. A. (1991). Primary and secondary effects of water content on the spectral reflectance of leaves. *American Journal of Botany*, *78*(7), 916−924.

Casals-carrasco, P., Kubo, S., & Madhavan, B. B. (2000). Application of spectral mixture analysis for terrain evaluation studies. *International Journal of Remote Sensing*, *21*, 3039−3055.

Chen, J. M., Leblanc, S. G., Cihlar, J., Desjardins, R. L., & MacPherson, J. I. (1999). Extending aircraft- and tower-based CO_2 flux measurements to a boreal region using a Landsat thematic mapper land cover map. *Journal of Geophysical Research, Atmospheres*, *104*(D14), 6859−16877.

Chen, X., Vierling, L., Rowell, E., & DeFelice, T. (2004). Using lidar and effective LAI data to evaluate IKONOS and Landsat 7 ETM+ vegetation cover estimates in a ponderosa pine forest. *Remote Sensing of Environment*, *91*, 14−26.

Choularton, T. W., Gallagher, M. W., Bower, K. N., Fowler, D., Zahniser, M., & Kaye, A. (1995). Trace gas flux measurements at the landscape scale using boundary layer budgets. *Philosophical Transactions of the Royal Society of London, Series A (Mathematical, Physical, and Engineering Sciences)*, *351*, 357−368.

Davis, K. J., Lenschow, D. H., & Zimmerman, P. R. (1994). Biogenic nonmethane hydrocarbon emissions estimated from tethered balloon observations. *Journal of Geophysical Research, Atmospheres*, *99*(D12), 25587−25598.

Elmore, A. J., Mustard, J. F., Manning, S. J., & Lobell, D. B. (2000). Quantifying vegetation change in semiarid environments: Precision and accuracy of spectral mixture analysis and the normalized difference vegetation index. *Remote Sensing of Environment*, *73*, 87−102.

Foody, G. M., & Cox, D. P. (1994). Sub-pixel land cover composition estimation using a linear mixture model and fuzzy membership functions. *International Journal of Remote Sensing*, *15*, 619−631.

Friedli, B., Tobias, S., & Fritsch, M. (1998). Quality assessment of restored soils: Combination of classical soil science methods with ground penetrating radar and near infrared aerial photography? *Soil and Tillage Research*, *46*, 103−115.

Gamon, J. A., Huemmrich, K. F., Peddle, D. R., Chen, J., Fuentes, D., Hall, F. G., et al. (2004). Remote sensing in BOREAS: Lessons learned. *Remote Sensing of Environment*, *89*, 139−162.

Garcia-Haro, F. J., Gilabert, M. A., & Melia, J. (1996). Linear spectral mixture modeling to estimate vegetation amount from optical spectral data. *International Journal of Remote Sensing*, *17*, 3373−3400.

Gerard, B., Buerkert, A., Hiernaux, P., & Marschner, H. (1997). Non-destructive measurement of plant growth and nitrogen status of pearl millet with low-altitude aerial photography. *Soil Science and Plant Nutrition*, *43*, 993−998.

Gilabert, M. A., Garcia-Haro, F. J., & Melia, J. (2000). A mixture modeling approach to estimate vegetation parameters for heterogeneous canopies in remote sensing. *Remote Sensing of Environment*, *72*, 328−345.

Greenberg, J. P., Guenther, A., Zimmerman, P., Baugh, W., Geron, C., Davis, K., et al. (1999). Tethered balloon measurements of biogenic VOCs in the atmospheric boundary layer. *Atmospheric Environment*, *33*(6), 855−867.

Guenther, A. (1997). Seasonal and spatial variations in natural volatile organic compound emissions. *Ecological Applications*, *7*, 34−45.

Guenther, A., Baugh, W., Davis, K., Hampton, G., Harley, P., Klinger, L., et al. (1996). Isoprene fluxes measured by enclosure, relaxed eddy accumulation, surface layer gradient, mixed layer gradient, and mixed layer mass balance techniques. *Journal of Geophysical Research, Atmospheres*, *101*(D13), 18555−18567.

Hansen, M. C., DeFries, R. S., Townshend, J. R. G., Sohlberg, R., Dimiceli, C., & Carroll, M. (2002). Towards an operational MODIS continuous field of percent tree cover algorithm: Examples using AVHRR and MODIS data. *Remote Sensing of Environment*, *83*, 303−319.

Huang, C., & Townshend, J. R. G. (2003). A stepwise regression tree for nonlinear approximation: Applications to estimating subpixel land cover. *International Journal of Remote Sensing*, *24*, 75−90.

Huete, A. R. (1986). Separation of soil–plant spectral mixtures by factor analysis. *Remote Sensing of Environment*, *19*, 237−251.

Jasinski, M. F., & Eagleson, P. S. (1990). Estimation of subpixel vegetation cover using red-infrared scattergrams. *IEEE Transactions on Geoscience and Remote Sensing*, *28*, 253−267.

Kootwijk, E. J. V., Van Der, Voet, H., & BerDowski, J. J. M. (1995). Estimation of ground cover composition per pixel after matching image and ground data with subpixel accuracy. *International Journal of Remote Sensing*, *16*, 97−111.

Kuck, L. R., Smith, T., Balsley, B. B., Helmig, D., Conway, T. J., Tans, P. P., et al. (2000). Measurements of landscape-scale fluxes of carbon dioxide in the Peruvian Amazon by vertical profiling through the atmospheric boundary layer. *Journal of Geophysical Research, Atmospheres*, *105*(D17), 22137−22146.

Lobell, D. B., Asner, G. P., Law, B. E., & Treuhaft, R. N. (2002). View angle effects on canopy reflectance and spectral mixture analysis of coniferous forests using AVIRIS. *International Journal of Remote Sensing*, *23*, 2247−2262.

Meer, F. V. D. (1995). Spectral unmixing of Landsat Thematic Mapper data. *International Journal of Remote Sensing*, *16*, 3189−3194.

Meer, F. V. D., & Jong, S. M. D. (2000). Improving the results of spectral unmixing of Landsat Thematic Mapper imagery by enhancing the orthogonality of end-members. *International Journal of Remote Sensing*, *21*, 2781−2797.

Monteiro, A. L., Souza Jr., C. M., & Barreto, P. (2003). Detection of logging in Amazonian transition forests using spectral mixture models. *International Journal of Remote Sensing*, *24*, 151−159.

North, P. R. J. (2002). Estimation of fAPAR, LAI, and vegetation fractional cover from ATSR-2 imagery. *Remote Sensing of Environment*, *80*, 114−121.

Ogunjemiyo, S. O., Kaharabata, S. K., Schuepp, P. H., MacPherson, I. J., Desjardins, R. L., & Roberts, D. A. (2003). Methods of estimating CO_2, latent heat and sensible heat fluxes from estimates of land cover fractions in the flux footprint. *Agricultural and Forest Meteorology*, *117*, 125−144.

Painter, T. H., Roberts, D. A., Green, R. O., & Dozier, J. (1998). The effect of grain size on spectral mixture analysis of snow-covered area from AVIRIS data. *Remote Sensing of Environment*, *65*, 320−332.

Peddle, D. R., Hall, F. G., & LeDrew, E. F. (1999). Spectral mixture analysis and geometric-optical reflectance modeling of boreal forest biophysical structure. *Remote Sensing of Environment*, *67*, 288−297.

Peterson, S. H., & Stow, D. A. (2003). Using multiple image endmember spectral mixture analysis to study chaparral regrowth in southern California. *International Journal of Remote Sensing*, *24*, 4481−4504.

Phinn, S., Stanford, M., & Scarth, P. (2002). Monitoring the composition of urban environments based on the vegetation–impervious surface–soil (VIS) model by subpixel analysis techniques. *International Journal of Remote Sensing*, *23*, 4131−4153.

Ray, T. W., & Murray, B. C. (1996). Nonlinear spectral mixing in desert vegetation. *Remote Sensing of Environment*, *55*, 59−64.

Ridd, M. K. (1995). Exploring a V–I–S (vegetation–impervious surface–soil) model for urban ecosystem analysis through remote sensing: Comparative anatomy for cities. *International Journal of Remote Sensing*, *16*, 2165−2186.

Roberts, D. A., Gardner, M., Church, R., Ustin, S., Scheer, G., & Green, R. R. (1998). Mapping chaparral in the Santa Monica Mountains using multiple endmember spectral mixture models. *Remote Sensing of Environment*, *65*, 267−279.

Roberts, D. A., Smith, M. O., & Adams, J. B. (1993). Green vegetation, non-photosynthetic vegetation, and soils in AVIRIS data. *Remote Sensing of Environment*, *44*, 255−269.

Rosin, P. L. (2001). Robust pixel unmixing. *IEEE Transactions on Geoscience and Remote Sensing*, *39*, 1978−1983.

Sabol, D. E., Gillespie, A. R., Adams, J. B., Smith, M. O., & Tucker, C. J. (2002). Structural stage in Pacific Northwest forests estimated using simple mixing models of multispectral images. *Remote Sensing of Environment*, *80*, 1−16.

Schowengerdt, R. A. (1997). *Remote sensing models and methods for image processing*, 2nd edition San Diego, CA: Academic Press Ltd.

Small, C. (2001). Estimation of urban vegetation abundance by spectral mixture analysis. *International Journal of Remote Sensing*, *22*, 1305−1334.

Spirig, C., Guenther, A., Greenberg, J. P., Calanca, P., & Tarvainen, V. (2004). Tethered balloon measurements of biogenic volatile organic compounds at a boreal forest site. *Atmospheric Chemistry and Physics*, *4*, 215−229.

Theseira, M. A., Thomas, G., & Sannier, C. A. D. (2002). An evaluation of spectral mixture modeling applied to a semi-arid environment. *International Journal of Remote Sensing*, *23*, 687−700.

Vierling, L. A., Fersdahl, M., Chen, X., Li, Z., & Zimmerman, P. (2006). The Short Wave Aerostat-Mounted Imager (SWAMI): A novel platform for acquiring remotely sensed data from a tethered balloon. *Remote Sensing of Environment*, *103*, 255−264 (this issue). doi:10.1016/j.rse.2005.01.021.

Vikhamar, D., & Solberg, R. (2003). Snow-cover mapping in forests by constrained linear spectral unmixing of MODIS data. *Remote Sensing of Environment*, *88*, 309−323.

Wessman, C. A., Bateson, C. A., & Benning, T. L. (1997). Detecting fire and grazing patterns in tallgrass prairie using spectral mixture analysis. *Ecological Applications*, *7*, 493−511.

Woodcock, C. E., & Strahler, A. H. (1987). The factor of scale in remote sensing. *Remote Sensing of Environment*, *21*, 311−332.

Wu, C., & Murray, A. T. (2003). Estimating impervious surface distribution by spectral mixture analysis. *Remote Sensing of Environment*, *84*, 493−505.

Zhang, L., Li, D., Tong, Q., & Zheng, L. (1998). Study of the spectral mixture model of soil and vegetation in PoYang Lake area, China. *International Journal of Remote Sensing*, *19*, 2077−2084.

Zimmerman, P. R., Greenberg, J. P., & Westberg, C. E. (1988). Measurements of atmospheric hydrocarbons and biogenic emission fluxes in the Amazon boundary layer. *Journal of Geophysical Research, Atmospheres*, *93*(D2), 1407−1416.